



Article

A Design of Vanadium Dioxide for Dynamic Color Gamut Modulation Based on Fano Resonance

Junyang Zhu, Ruimei Zeng , Yiwen Yang, Yiqun Zhou, Zhen Gao, Qi Wang * , Ruijin Hong and Dawei Zhang

Shanghai Key Laboratory of Modern Optics System, Engineering Research Center of Optical Instrument and System, Ministry of Education and Shanghai Key Laboratory of Modern Optics System, School of Optical-Electrical and Computer Engineering, University of Shanghai for Science and Technology, 516 Jungong Rd, Shanghai 200093, China; zjy20000107@163.com (J.Z.); z224994@163.com (R.Z.); y2021051129@163.com (Y.Y.); zyzq2018990225@163.com (Y.Z.); 18916428395@163.com (Z.G.); rjhong@usst.edu.cn (R.H.); dwzhang@usst.edu.cn (D.Z.)

* Correspondence: shelly3030@163.com

Abstract: In this paper, a design of vanadium dioxide for dynamic color gamut modulation based on Fano resonance is proposed. This approach facilitates color modulation by manipulating the phase transition state of vanadium dioxide. The device integrates both broadband and narrowband filters, featuring a structure consisting of a top silver mesh, a layer of vanadium dioxide, and a Fabry–Pérot cavity, which allows for effective modulation of the reflectance spectrum. Simulation results demonstrate that when vanadium dioxide is in its insulating state, the maximum reflectivity observed in the device spectrum, reaching 43.1%, appears at 475 nm. Conversely, when vanadium dioxide transitions to its metallic state, the peak wavelength shifts to 688 nm, accompanied by an increased reflectance peak of 59.3%. Analysis of electric field distributions reveals that the intensity caused by surface plasmonic resonance dominates over the excited Fano resonance while vanadium dioxide is in its insulating state, which is the opposite of when vanadium dioxide transitions to its metallic state. This behavior exhibits an excellent dynamic color-tuning capability. Specifically, the phase transition of vanadium dioxide results in a color difference ΔE_{2000} of up to 36.7, while maintaining good color saturation. This technique holds significant potential for applications such as dynamic color display and anti-counterfeit labeling.



Citation: Zhu, J.; Zeng, R.; Yang, Y.; Zhou, Y.; Gao, Z.; Wang, Q.; Hong, R.; Zhang, D. A Design of Vanadium Dioxide for Dynamic Color Gamut Modulation Based on Fano Resonance. *Crystals* **2024**, *14*, 1096. <https://doi.org/10.3390/cryst14121096>

Academic Editor: Dmitri Donetski

Received: 21 November 2024

Revised: 7 December 2024

Accepted: 18 December 2024

Published: 19 December 2024



Copyright: © 2024 by the authors. Licensee MDPI, Basel, Switzerland. This article is an open access article distributed under the terms and conditions of the Creative Commons Attribution (CC BY) license (<https://creativecommons.org/licenses/by/4.0/>).

Keywords: vanadium dioxide; Fano resonance; phase transition; color display

1. Introduction

Traditional chemical pigments have been widely utilized since ancient times due to their advantages of simple production and low cost. However, with societal advancements, traditional chemical pigments characterized by low color saturation, low brightness, and heavy pollution are gradually becoming inadequate for meeting the demands for rapid progress in color display, anti-counterfeiting, and other applications. To address these challenges, various artificial micro-nano structures, such as multilayer thin films [1–5], thin film nanocavities [6–8], plasma nanostructures [9,10], dielectric nanostructures [11–13], and photonic crystals [14,15] have been employed. These structures can interact with incident light on a subwavelength scale, enabling modulation of the reflected/incident light spectrum by modulating the various resonances involved in the excitation processes. The color filters fabricated using these methods exhibit capabilities for generating a wide range of structural colors while offering high color saturation and brightness. Consequently, they are gradually replacing traditional chemical coloring techniques in the fields such as color printing [16–18], optical anti-counterfeiting [19,20], data encryption [21,22], data storage [23], display technology [24–28], and photovoltaic cells [29].

Typically, color filters based on micro-nano structures utilize metal plasmonic resonance [30], Fabry–Pérot (FP) resonance, or guided mode resonance to generate colors.

However, these spectra often encounter challenges in further narrowing the full width at half maximum (FWHM) and peak value of the resonance spectra to improve both color saturation and brightness. In recent years, researchers have increasingly emphasized the application of Fano resonance for color display. By combining a broadband filter with a narrowband filter, the excitation of Fano resonance produces a well-known asymmetric line shape characterized by a sharp peak and high intensity. Elkabbash et al. [31] investigated the structural coloring properties of Fano resonance optical coatings (FROCs) and designed FROC devices consisting of silver (Ag)-germanium (Ge)-titanium dioxide (TiO₂)-Ag, utilizing FP cavities along with absorbing thin films of Ge to achieve the desired Fano resonance. The incorporation of a silicon dioxide layer to suppress short-wavelength band reflections significantly improves the color purity (up to 99%) and expands color range coverage (up to 61% of the CIE color space). Chen et al. [32] explored the Fano resonance achieved by embedding a monolayer of tungsten disulfide (WS₂) within an FP cavity, successfully demonstrating the Fano resonance phenomenon. Through the numerical study of coupled mode theory (CMT) and the finite difference time domain method (FDTD), it was determined that the coupling strength for Fano resonance could reach 14.1 meV due to the large dipole jump moments of WS₂. By adjusting parameters such as the height of the FP cavity, the position of the WS₂ monolayer, and the refractive index of the medium in the FP cavity, the Fano resonance line shape could be manipulated, and the peak transmittance of the device reached up to 55%.

However, these designed color filters need to alter the color response of the device by changing the structural parameters, which means that once fabricated, these devices are limited to producing fixed colors, which poses challenges in meeting flexible and practical demands. Therefore, dynamic color gamut devices are garnering increasing attention. Phase change materials (PCMs), such as antimony trisulfide (Sb₂S₃), diantimony triselenide (Sb₂Se₃), and vanadium dioxide (VO₂), can alter their refractive indices simply through temperature changes, causing the change for optical properties of the device. This characteristic has led PCM-Fano resonance optical coatings integrated with phase change materials to become popular among researchers. Huang et al. [33] integrated the PCM material Sb₂Se₃ into FROC systems, enabling tunable structural colors in both reflection and transmission modes through photonic Fano resonance. The color gamut of this four-layer thin-film optical coating could cover red, green, and blue, achieving peak reflections of up to 80%. However, the device exhibited poor color saturation. Prabhathan et al. [34] proposed a steganographic nano-optical coating (SNOC), utilizing Sb₂S₃ to achieve color-tunable optical Fano resonance, resulting in the dynamic tuning across the full-color gamut within the visible wavelength range, with peak reflectance reaching 78%, and demonstrating the capability to display the full-color gamut. These devices have a common defect: the limitation observed in these devices is their restricted dynamic color rendering range, which means the color difference caused by the PCM phase change is minimal.

In this paper, we proposed a design of VO₂ for dynamic color gamut modulation based on Fano resonance. By utilizing the excited Fano resonance peak, the color difference produced by the VO₂ phase transition can be improved while ensuring good color saturation of the color produced by the device, which demonstrates its stronger capability for dynamic color rendering than that of the existing VO₂ color filters. Specifically, the phase transition of VO₂ results in a color difference ΔE_{2000} of up to 36.7, while maintaining good color saturation. Simulated spectral and electric field results demonstrate the superiority of this technique. Based on the above results, we designed a simple pattern to explore the initial applications of this technique, demonstrating its significant potential for research fields such as dynamic color display and anti-counterfeit labeling.

2. Materials and Methods

2.1. Fano Resonance

When a resonance characterized by broader spectral range and a resonance characterized by narrower spectral range couple in the near field, they can lead to destructive interference, resulting in sharp asymmetric features in the spectral lines [35], which is referred as Fano resonance [31,36]. The Fano fitting formula can be described by Equation (1) [37].

$$\sigma = \frac{(q + \varepsilon)^2}{1 + \varepsilon^2} \quad (1)$$

In Equation (1), σ represents the absorption spectrum of Fano resonance. q denotes the asymmetric parameter of the Fano resonance spectral line. ε is defined as $2(E - E_F)/\Gamma$, where E_F is the resonance energy and Γ is the width of the resonance spectral line.

2.2. Optical Properties of VO₂

VO₂ has been extensively studied since its discovery in 1959 [38]. The phase transition properties of VO₂ have garnered significant interest among researchers [39], as illustrated by the refractive index curves before and after the phase transition depicted in Figure 1. VO₂ remains in an insulating state below 68 °C (341 K); however, it undergoes a phase transition from insulator(I) to metal(M) when the temperature exceeds this critical threshold. This transition is accompanied by a significant decrease in the refractive index when VO₂ enters its metallic state. Such optical properties offer opportunities for designing dynamic gamut color filters. Furthermore, the relatively low phase transition temperature of VO₂ compared to other PCMs means that it requires fewer conditions for initiating the phase transition, thereby expanding its applicability in optical design.

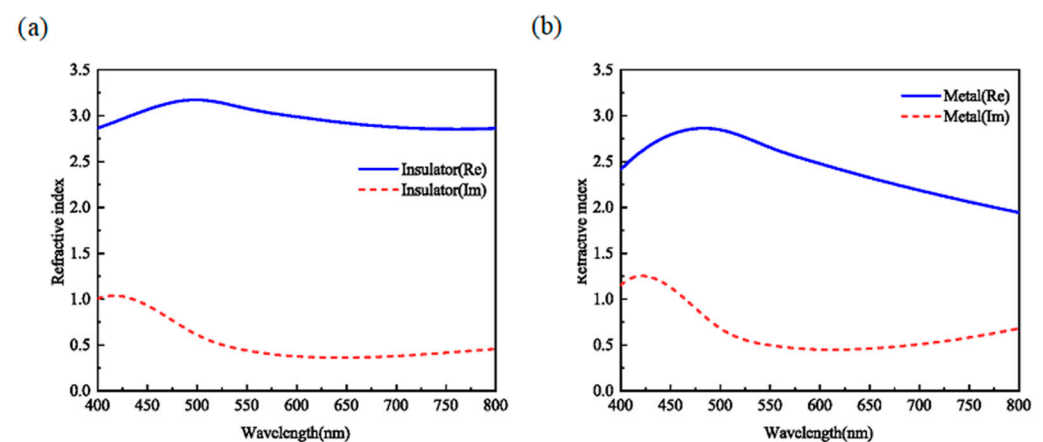


Figure 1. Refractive index of VO₂, (a) in the insulating state, (b) in the metallic state.

3. Structure and Design

The FROC device designed in this paper is illustrated in Figure 2. Figure 2a,b present the top view and front view of the device for a single period, respectively, and Figure 2c shows the schematic of the device configured for multiple periods to form an array. The device consists of an Ag mesh, a VO₂ layer, an Ag layer, a silicon (Si) layer, and an Ag substrate layer arranged sequentially from top to bottom. The period P is set at 200 nm, length L is 180 nm, heights h_1 , h_2 , and h_3 are all maintained at 40 nm, height h_4 is specified as 50 nm, and substrate thickness h_5 is 200 nm. The structure was simulated using FDTD Solutions with material data from Palik [40] and Rakić [41]. Mesh sizes (dx , dy , dz) were uniformly maintained at 3 nm throughout the simulation process. The device is illuminated by transverse magnetic (TM) light.

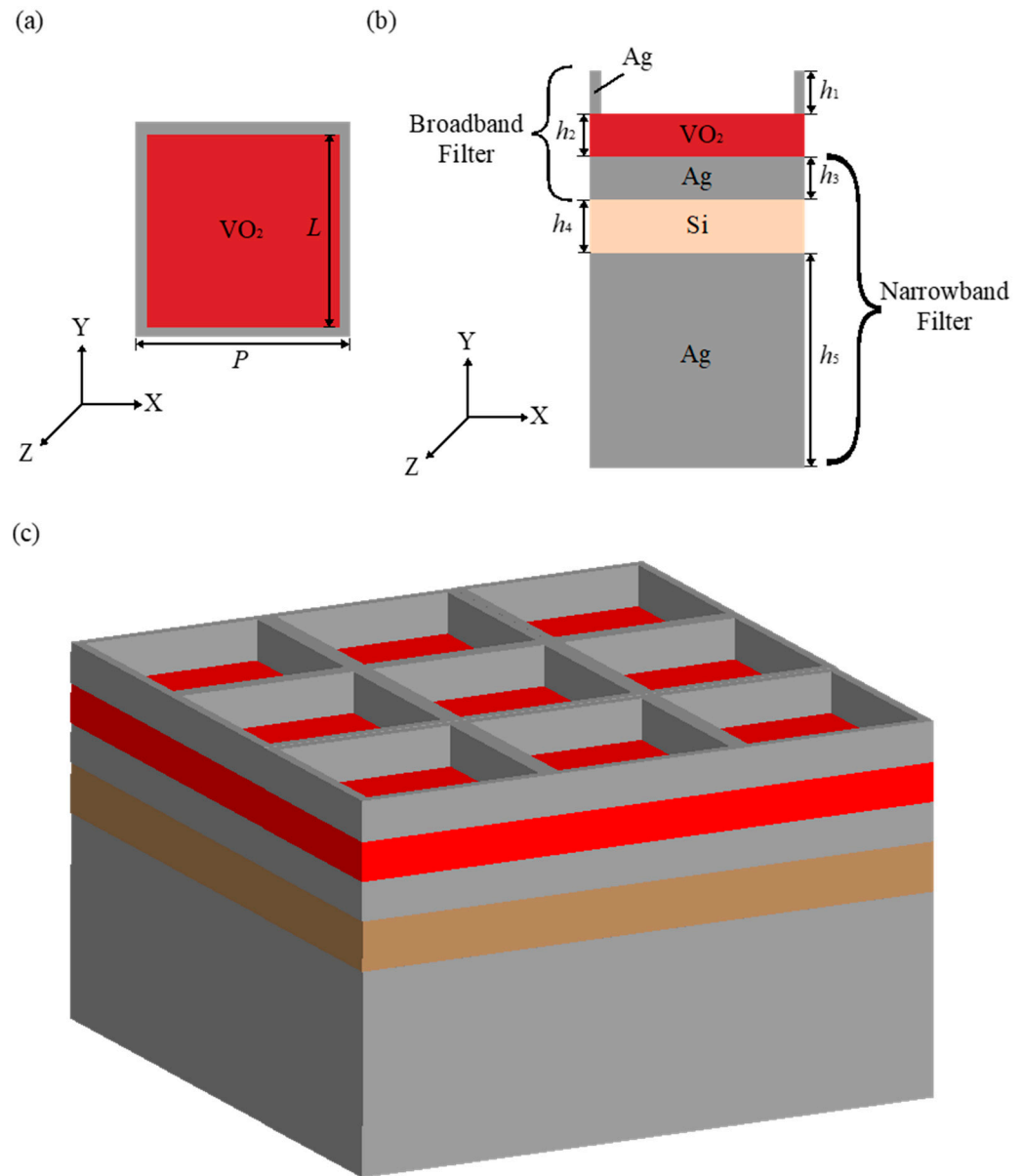


Figure 2. Structure of the designed FROC; (a) top view, (b) front view. (c) Schematic of the FROC array.

4. Results and Analysis

The FROC device may consist of a broadband filter and a narrowband filter. The reflection spectrum of the broadband filter and the narrowband filter are shown in Figure 3. The broadband filter consists of a meshed Ag layer, VO₂ layer, and Ag layer, as depicted in the upper part of Figure 2b. This filter utilizes an SPR, which generates a broad valley in the spectrum, and causes a significant change with the phase transition of VO₂ changes. As shown in Figure 3a, when VO₂ is in its insulating state, the trough of the reflection spectrum is located at 673 nm, whereas after the VO₂ phase transition, the trough of the spectrum is blue-shifted to 591 nm, and such a spectral change provides the basis for the dynamic color-rendering performance of the FROC device. Conversely, the narrowband filter consists of an Ag layer, Si layer, and Ag layer, as depicted in the bottom part of Figure 2b, which is a classical FP cavity resonance structure. By varying the thickness of the silicon layer, the thickness of the FP cavity can be varied and the reflection spectrum shifted. As shown in Figure 3b, the narrowband filter produces two distinct troughs, one located at approximately 418 nm with a trough reflectance value of around 51% and another at about 711 nm with a trough value near 19%.

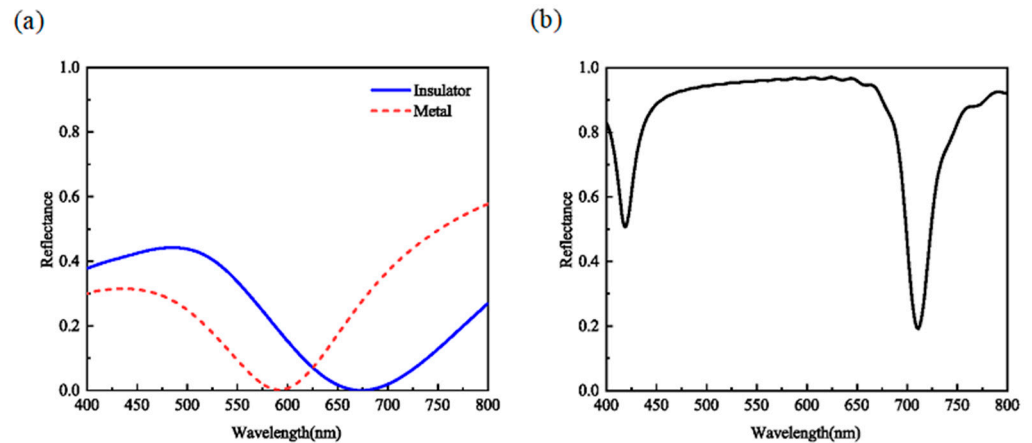


Figure 3. Reflection spectrum of (a) broadband filter, (b) narrowband filter.

The reflectance spectra of the FROC device are presented in Figure 4a, demonstrating variations induced by changes in the device temperature that facilitate phase transitions in VO_2 . This spectral result exhibits an asymmetric line characteristic of Fano resonance phenomena in the long-wavelength region of the spectrum. A comparative analysis with the reflection spectra from both broadband and narrowband filters indicates that within the short-wavelength region of the visible spectrum, the reflection spectra of the device primarily originated from the upper broadband filter, and there is minimal impact on performance due to a trough observed around 440 nm in the narrowband filter. In contrast, within the long-wavelength range of the visible spectrum, both the two filters are effectively coupled to excite Fano resonance effects, resulting in resonance peaks appearing at wavelengths of approximately 695 nm and 688 nm, with a reflectance peak reaching up to 40.2% when VO_2 exists in its insulating state and increasing to 59.3% when it transitions into its metallic state, respectively. Their corresponding chromaticity coordinates have been calculated from the spectral data and plotted in the CIE1931 chromaticity diagram. As illustrated in Figure 4b, by modulating the phase transition state of VO_2 , the device demonstrates its capability to reflect two distinct colors, blue and fuchsia, with a chromatic difference ΔE_{2000} as high as 36.7. Compared with the existing FROC design, this device can maintain good color saturation while maintaining an excellent dynamic color rendering range.

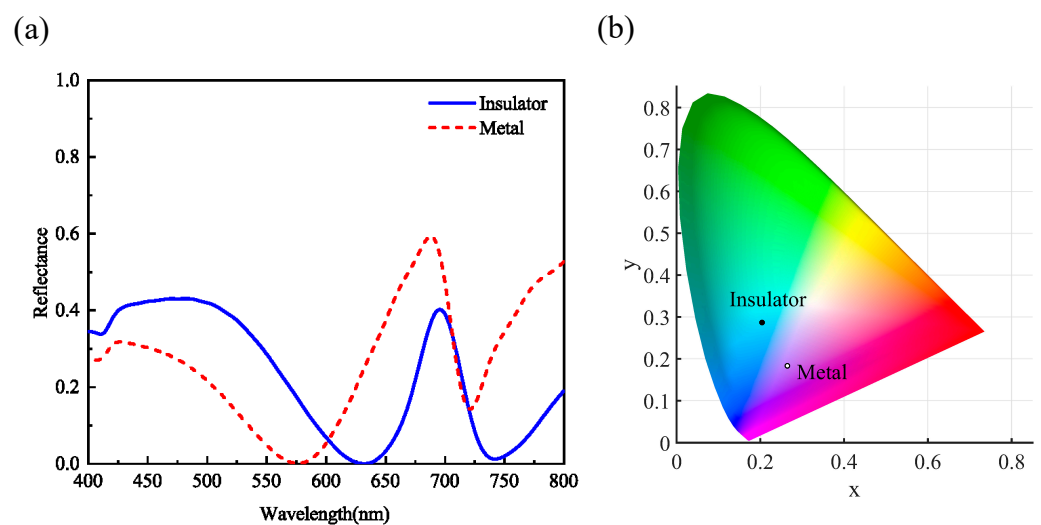


Figure 4. (a) Reflection spectrum when incident light vertically irradiates. (b) Chromaticity coordinates marked in the CIE1931 chromaticity diagram according to the spectrum shown in (a).

The variation in the thickness of the VO_2 layer (h_2) from 20 nm to 60 nm at a step of 10 nm significantly influences the reflectance spectra of the broadband filter, as illustrated

in Figure 5a. The corresponding results for the reflectance spectra of the FROC device are presented in Figure 5b. As the thickness of VO₂ increases, a red shift is observed in the spectrum, which serves as a primary factor influencing the short-wavelength band spectrum of the FROC device. The increase in the thickness of the broadband filter leads to enhanced absorption and reflection, resulting in reduced energy leakage to the lower narrowband filter. Consequently, this suppression diminishes Fano resonance within the long-wavelength band of the FROC device, leading to a notable decrease in its long-wavelength band reflectance. The corresponding chromaticity coordinates derived from the spectral data of Figure 5b are plotted in the CIE1931 chromaticity diagram, as depicted in Figure 5c. When the VO₂ layer is in the insulating state and its thickness varies from 20 nm to 60 nm at a step of 10 nm, sequentially calculated chromaticity coordinates are (0.500, 0.360), (0.297, 0.204), (0.205, 0.297), (0.278, 0.345), and (0.316, 0.348). In contrast, when the VO₂ layer transitions into the metallic state with varying thickness from 20 nm to 60 nm, these chromaticity coordinates are (0.458, 0.370), (0.469, 0.267), (0.264, 0.185), (0.196, 0.272), and (0.233, 0.317). It is evident that the color variation within this range for the FROC device follows an order from orange through red, then to purple, blue, and green while exhibiting decreased saturation, particularly within the green region.

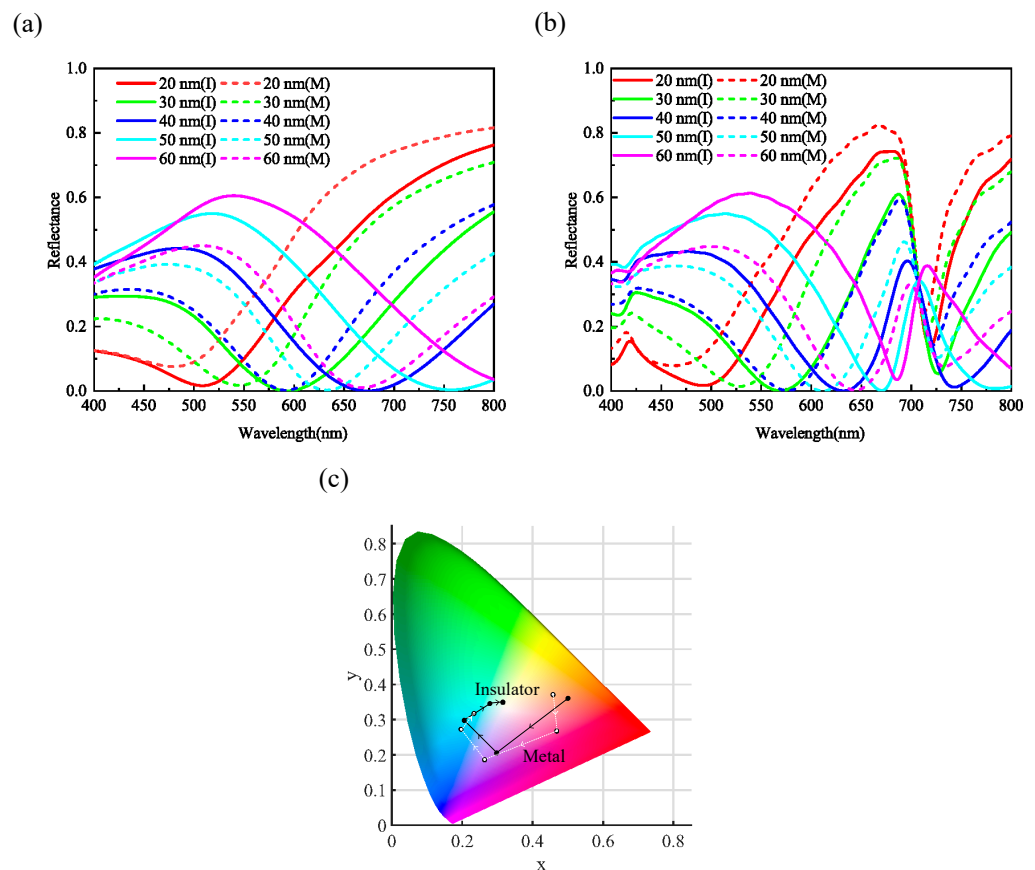


Figure 5. Reflection spectra (a) of the broadband filter (upper part of the FROC), (b) of the FROC, when h_2 is varied from 20 nm to 60 nm at a step of 10 nm. (c) Chromaticity coordinates marked in the CIE1931 chromaticity diagram according to the spectrum shown in (b). The black solid lines show the movement trajectory of the chromaticity coordinates when VO₂ is in its insulating state, and the white dashed lines show the movement trajectory of the chromaticity coordinates when VO₂ is in its metallic state.

As illustrated in Figure 6a, the variation in the Ag layer thickness (h_3) from 10 nm to 40 nm at a step of 10 nm significantly influences the reflection spectra of the FROC device. Similar to the effects observed with variations in the thickness of the VO₂ layer

(h_2), an increase in the thickness of the Ag layer (h_3) leads to enhanced absorption and reflection, which results in a significant reduction in the intensity of Fano resonance. The corresponding chromaticity coordinates are derived from the spectral data and plotted in the CIE1931 chromaticity diagram, as depicted in Figure 6b. When VO₂ is in its insulating state, the reflected colors change from the purplish-red region to the blue region. Conversely, when VO₂ transitions into its metallic state, the color coordinates shift leftward, while remaining within the violet-red region.

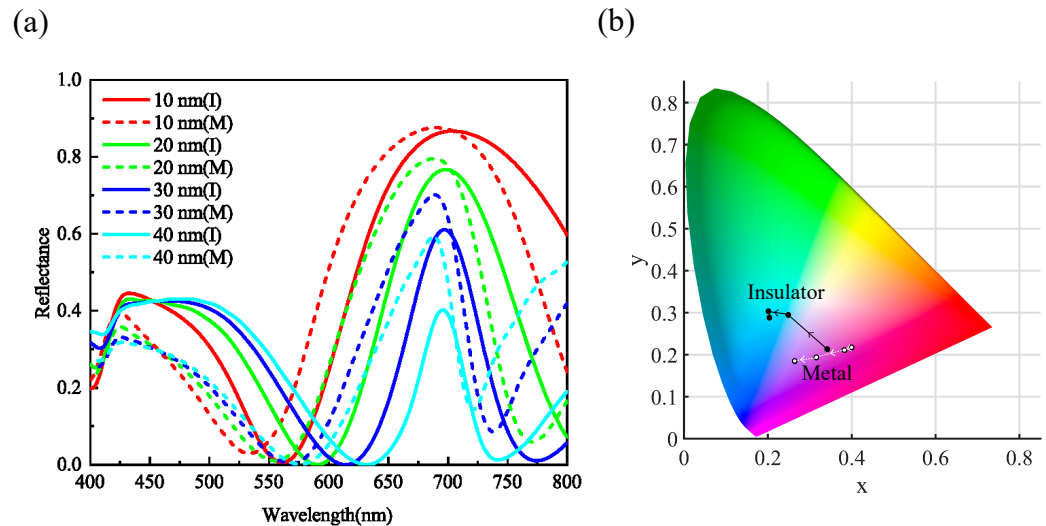


Figure 6. (a) Reflection spectrum of the FROC when h_3 is varied from 10 nm to 40 nm at a step of 10 nm. (b) Chromaticity coordinates marked in the CIE1931 chromaticity diagram according to the spectrum shown in (a). The black solid lines show the movement trajectory of the chromaticity coordinates when VO₂ is in its insulating state, and the white dashed lines show the movement trajectory of the chromaticity coordinates when VO₂ is in its metallic state.

The reflectance spectra of the broadband filter are presented in Figure 7a as the length L of the top square mesh is varied from 190 nm to 130 nm at a step of 10 nm. The results for the reflectance spectra of the FROC device are shown in Figure 7b. The length of L was altered to change the duty cycle of the silver mesh while maintaining a constant period P . The duty cycle is defined as $D = 1 - (\frac{L}{P})^2$, where L is the length of the square mesh and P is the period of the device. As L decreases, the duty cycle gradually increases, which leads to both a blue shift in the spectrum and an increased reflectance intensity for the broadband filter. The reflectance spectrum of the FROC exhibits a similar trend to that observed with the broadband filter; however, it is noteworthy that while its position remains essentially unchanged, this pertains specifically to where Fano resonance peaks occur within the long-wavelength band. The corresponding chromaticity coordinates derived from the spectral data depicted in Figure 7b have been calculated and plotted in the CIE1931 chromaticity diagram, as illustrated in Figure 7c. When VO₂ is in its insulating state and L decreases from 190 nm to 130 nm at a step of 10 nm, the sequentially recorded chromaticity coordinates for the FROC are (0.220, 0.315), (0.204, 0.287), (0.200, 0.264), (0.228, 0.372), (0.228, 0.239), (0.242, 0.242), and (0.264, 0.243). And when VO₂ transitions into its metallic state, the chromaticity coordinates are (0.267, 0.193), (0.264, 0.183), (0.268, 0.185), (0.345, 0.337), (0.279, 0.210), (0.288, 0.226), and (0.314, 0.239). The colors reflected from the device predominantly fall within both blue and fuchsia regions. It is worth noting that when L is set to 160 nm, the device reflects blue-green (insulating state), and yellowish (metallic state), exhibiting a color difference ΔE_{2000} up to 28.1.

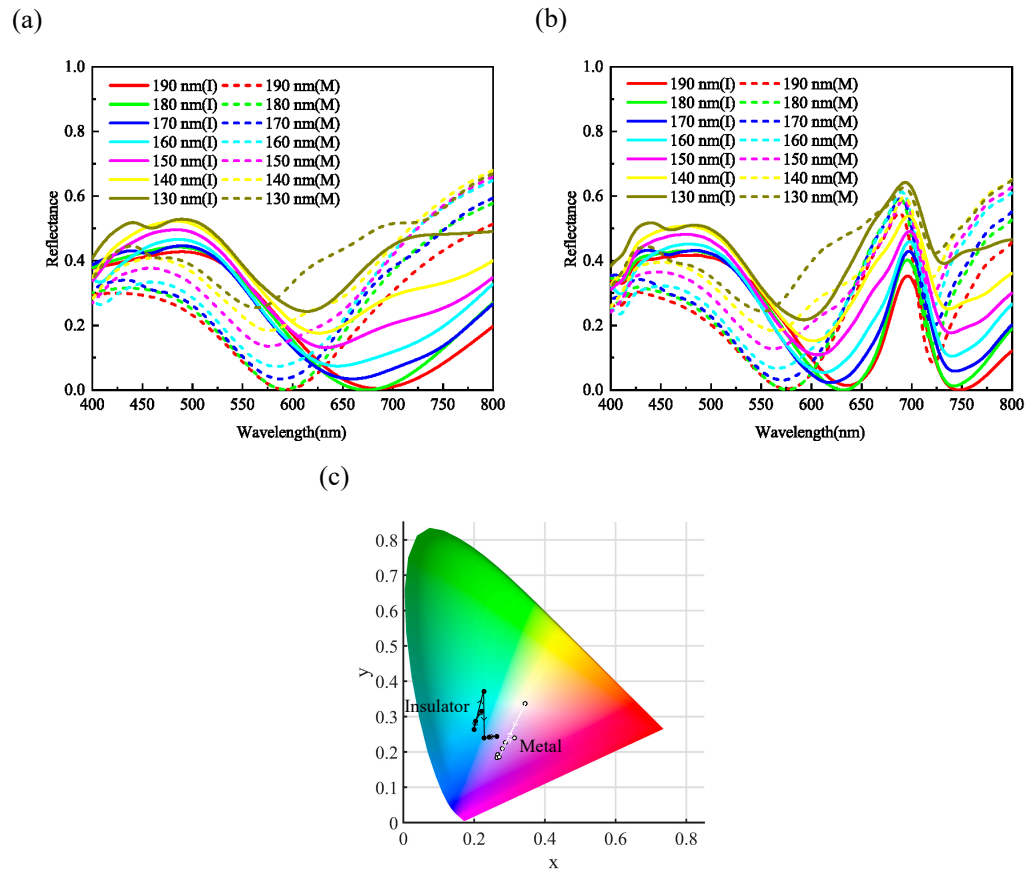


Figure 7. Reflection spectra (a) of the upper broadband filter, (b) of the FROC, when L is varied from 190 nm to 130 nm at a step of 10 nm. (c) Chromaticity coordinates marked in the CIE1931 chromaticity diagram according to the spectrum shown in (b). The black solid lines show the movement trajectory of the chromaticity coordinates when VO_2 is in its insulating state, and the white dashed lines show the movement trajectory of the chromaticity coordinates when VO_2 is in its metallic state.

Varying the thickness of the Si layer (h_4), we observed that as the thickness of the Si layer increases from 30 nm to 70 nm at a step of 10 nm, the reflection spectra of the narrowband filter are as shown in Figure 8a. The results of the reflection spectra of the FROC devices are shown in Figure 8b. A red shift occurs in the narrowband filter spectra with the increase in the Si layer, accompanied by an enlargement of the reflection troughs located within the short-wavelength band. In contrast, a similar red shift is observed for the position of the Fano resonance peak within the reflection spectrum of the FROC, when compared to that of the narrowband filter. Their corresponding chromaticity coordinates were calculated from the spectral data of Figure 8b and plotted in the CIE1931 chromaticity diagram, as illustrated in Figure 8c. When VO_2 is in its insulating state and h_4 increases from 30 nm to 70 nm at a step of 10 nm, the sequentially recorded chromaticity coordinates for FROC are (0.283, 0.271), (0.219, 0.222), (0.204, 0.287), (0.212, 0.300), and (0.220, 0.300). And when VO_2 transitions into its metallic state, the chromaticity coordinates are (0.247, 0.239), (0.295, 0.181), (0.264, 0.183), (0.234, 0.182), and (0.225, 0.208). Although variations in the thickness of the Si layer significantly affect the reflectance spectrum of the device, they exert only a minor influence on the color coordinates of the device; thus, it can be concluded that the colors of the FROC predominantly reside within blue (insulating state) versus fuchsia (metallic state) regions.

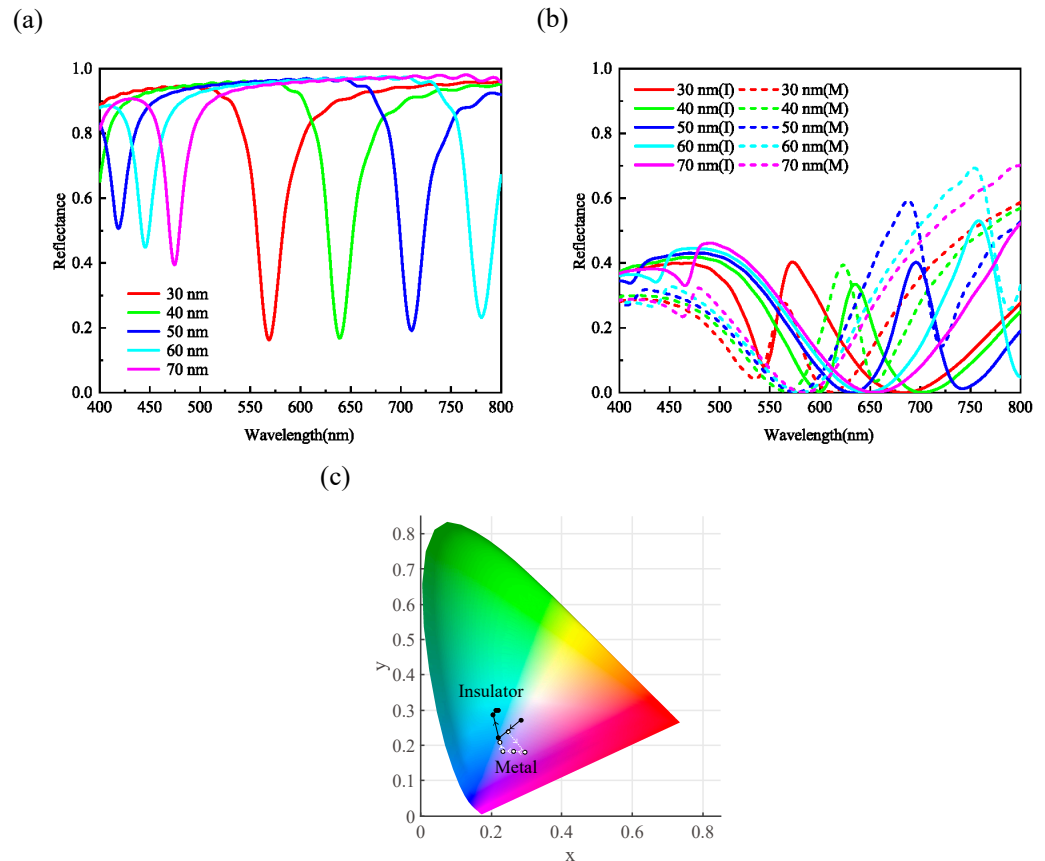


Figure 8. Reflection spectra (a) of the upper broadband filter, (b) of the FROC, when h_4 is varied from 30 nm to 70 nm at a step of 10 nm. (c) Chromaticity coordinates marked in the CIE1931 chromaticity diagram according to the spectrum shown in (b). The black solid lines show the movement trajectory of the chromaticity coordinates when VO_2 is in its insulating state, and the white dashed lines show the movement trajectory of the chromaticity coordinates when VO_2 is in its metallic state.

To elucidate the underlying physics of the FROC, the electric field distributions of both the broadband filter and FROC were calculated separately in the x - z plane for both insulator and metal states of VO_2 . The results are illustrated in Figure 9. The broadband filter located in the upper layer excites the SPR, which generates a strong electric field distribution at the corners of the silver mesh. In comparison to Figure 9a, the resonance that appeared in Figure 9b is weaker, as 688 nm is farther away from the resonant wavelength (591 nm) of the SPR. When the FROC is assembled, partial energy transmits through the mid-Ag layer, leading to FP resonance within the narrowband filter; this leads to an extra-strong electric field appearing at the top of the broadband filter. Combined with the asymmetric line shape observed in its spectrum, this phenomenon confirms that our device effectively excites Fano resonance. Notably, the Fano resonance depicted in Figure 9d exhibits greater strength than that shown in Figure 9c. Fano resonance facilitates transmission of the electric field energy across different cycles within this structure, significantly influencing reflectance spectra. When VO_2 is insulating, SPR predominates over the excited Fano resonance; thus, it primarily affects the entire reflection spectra with a maximum reflectivity reaching 43.1% located at 475 nm. Conversely, when VO_2 transitions to its metallic state, Fano resonance takes precedence within these spectra, demonstrating a peak reflectance reaching up to 59.3% at a wavelength of 688 nm. The substantial alteration observed within these spectra leads to a significant color difference before and after the FROC phase change. This phenomenon explains the excellent dynamic color rendering capability of the device.

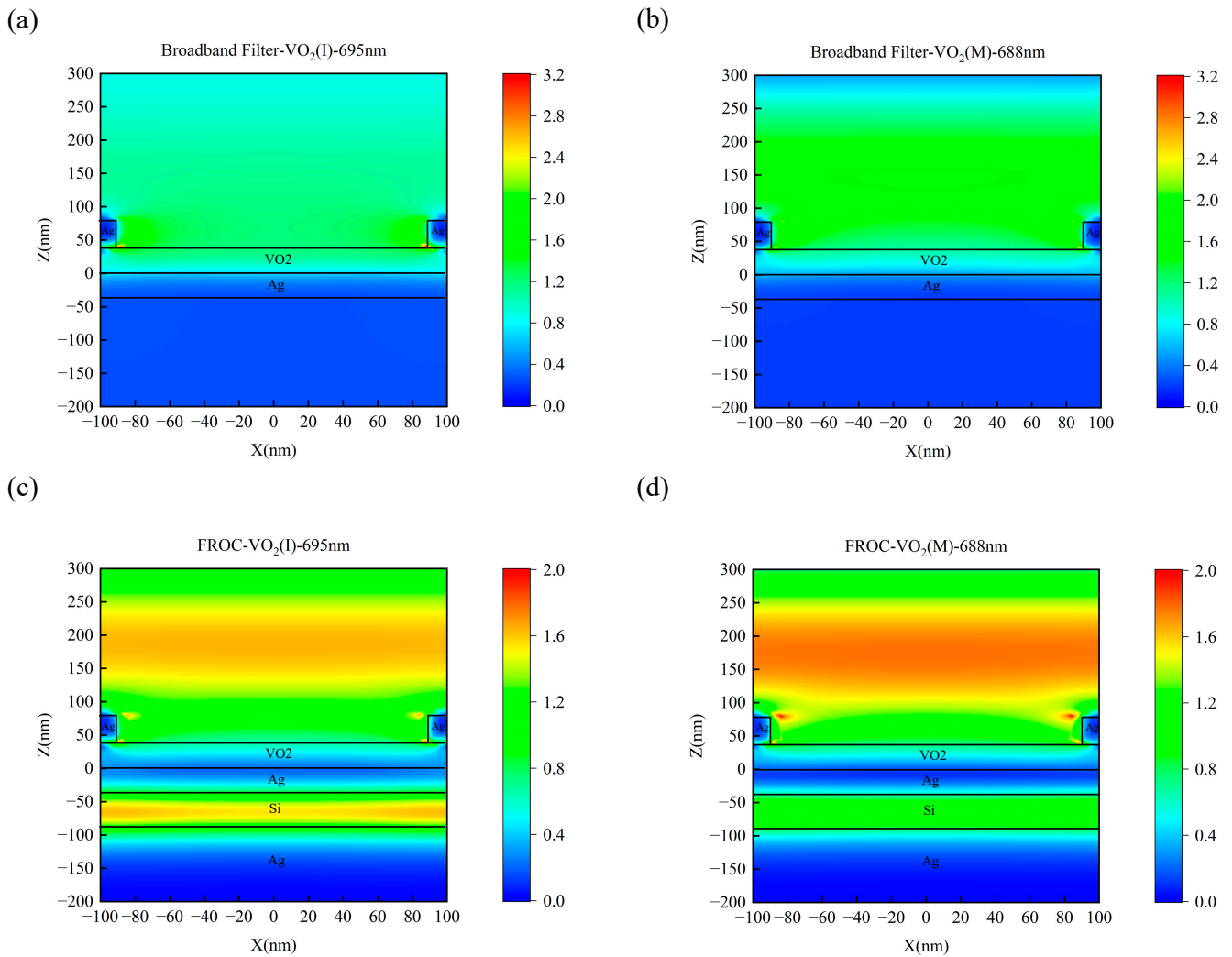


Figure 9. Electric field distributions of the broadband filter in the x-z plane; (a) wavelength of 695 nm light normally illustrated on VO₂ (insulating state); (b) wavelength of 688 nm light vertically irradiates on VO₂ (metallic state). Electric field distributions of the FROC in the x-z plane; (c) wavelength of 695 nm light vertically irradiates on VO₂ (insulating state); (d) wavelength of 688 nm light vertically irradiates on VO₂ (metallic state). The structures of the broadband filter and FROC depicted by the solid black lines are shown in the figure.

Based on the aforementioned analysis of the FROC performance, the device is initially investigated for applications in color display and anti-counterfeiting. As shown in Figure 10a, the pattern of “USST” consists of FROC arrays, where L is set to 160 nm while the remaining sections of the square grid are left unprepared (L is set to 0). The “USST” pattern becomes distinctly visible when VO₂ is in its metallic state; however, it nearly completely vanishes after the heating phase transition. This observation indicates that when VO₂ is in its metal state, the “USST” character is obvious, whereas after undergoing a phase change, the pattern almost entirely disappears. This phenomenon highlights the potential application of the device in the field of anti-counterfeiting. As depicted in Figure 10b, by merely varying the length L of the square grid (190 nm vs. 160 nm) along with the temperature adjustments, the device can reflect four distinct colors, blue, purple, green, and yellowish, which shows the potential utility of the device in color display applications.

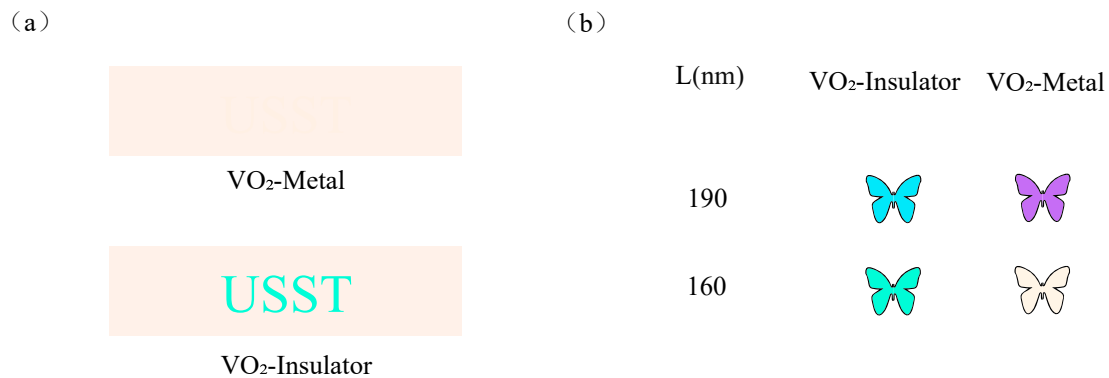


Figure 10. (a) “USST” pattern arranged by the array of the designed FROCs, which can be reversibly switched between visible and invisible by changing the temperature. The yellowish area is reflected by the structures without the top square grids (L is set as 0). (b) Butterfly patterns when VO_2 is in the insulating or metallic state and the length L is set as 190 nm or 160 nm, respectively.

5. Conclusions

In this paper, we proposed a design for VO_2 that facilitates dynamic color gamut modulation based on Fano resonance. This device achieves color modulation by manipulating the phase transition state of VO_2 , which combines both broadband and narrowband filters. Simulation results indicate that when the VO_2 is in its insulating state and metallic state, respectively, the maximum reflectivity of the device is observed at 475 nm (reaching 43.1%) and 688 nm (reaching 59.3%), respectively. This phenomenon exhibits that the design enables an excellent dynamic color tuning capability with a color difference ΔE_{2000} reaching up to 36.7, while maintaining good color saturation. Electric field distribution analysis reveals that the SPR intensity is stronger than that of the excited Fano resonance when VO_2 is in its insulating state; conversely, Fano resonance predominates the spectrum when VO_2 transitions to its metallic state. A dynamic color display can be achieved through the formation of arrays of FROC devices. A “USST” pattern has been developed, which can be reversibly switched between visibility and invisibility by altering temperature, thereby offering new possibilities for anti-counterfeit labels. Furthermore, this device exhibits the ability to display a wide range of colors, including blue, fuchsia, green, and pale yellow by simply varying either the length L of the square grid or adjusting the temperature of the device. In summary, this study demonstrates a novel FROC device that not only enables dynamically tunable reflective colors, but also provides extensive applications, such as color display and anti-counterfeiting.

Author Contributions: Conceptualization, J.Z. and Q.W.; methodology, Q.W.; software, J.Z., R.Z., Y.Y., Y.Z. and Z.G.; validation, J.Z., Q.W., R.H. and D.Z.; data curation, J.Z., R.Z., Y.Y. and Y.Z.; writing—original draft preparation, J.Z.; writing—review and editing, J.Z. and Q.W.; visualization, J.Z., Y.Y. and Z.G.; supervision, R.H. and D.Z.; project administration, Q.W.; funding acquisition, Q.W. All authors have read and agreed to the published version of the manuscript.

Funding: This research was funded by National Natural Science Foundation of China, grant number 62375175, and the national key research and development program of China, grant number 2022YFB2804602.

Data Availability Statement: The raw data supporting the conclusions of this article will be made available by the authors upon request.

Acknowledgments: The authors thank the University of Shanghai’s Science and Technology Department for providing administrative and technical support.

Conflicts of Interest: The authors declare no conflicts of interest.

References

1. Zhang, Y.; Zhou, Q.; Ai, R.; Li, X.; Li, L.; Han, Q. Luminescence enhancement of Y_2O_3 thin films based on LSPR effect of Ag nanolayers. *J. Alloys Compd.* **2024**, *988*, 174257. [[CrossRef](#)]
2. Kristensen, A.; Yang, J.; Bozhevolnyi, S.I.; Link, S.; Nordlander, P.; Halas, N.J.; Mortensen, N.A. Plasmonic colour generation. *Nat. Rev. Mater.* **2016**, *2*, 16088. [[CrossRef](#)]
3. Chen, S.; Rossi, S.; Shanker, R.; Cincotti, G.; Gamage, S.; Kühne, P.; Stanishev, V.; Engquist, I.; Berggren, M.; Edberg, J.; et al. Tunable Structural Color Images by UV-Patterned Conducting Polymer Nanofilms on Metal Surfaces. *Adv. Mater.* **2021**, *33*, 2102451. [[CrossRef](#)] [[PubMed](#)]
4. Lee, J.; Yu, E.S.; Kim, T.; Kim, I.S.; Chung, S.; Kwak, S.J.; Lee, W.B.; Pak, Y.; Ryu, Y.S. Naked-eye observation of water-forming reaction on palladium etalon: Transduction of gas-matter reaction into light-matter interaction. *Photonix* **2023**, *4*, 20. [[CrossRef](#)]
5. Moradinezhad, F.; Aliabadi, M.; Ansarifar, E. Zein Multilayer Electrospun Nanofibers Contain Essential Oil: Release Kinetic, Functional Effectiveness, and Application to Fruit Preservation. *Foods* **2024**, *13*, 700. [[CrossRef](#)]
6. Wen, J.; Chen, X.; Zhu, Z.; Zhu, Y.; Luo, H.; Wang, Y.; Liu, Y.; Wang, H.; Yuan, W.; Zhang, Y.; et al. Thin film-based colorful radiative cooler using diffuse reflection for color display. *Photonix* **2023**, *4*, 25. [[CrossRef](#)]
7. Lee, Y.; Yun, J.; Seo, M.; Kim, S.J.; Oh, J.; Kang, C.M.; Sun, H.J.; Chung, T.D.; Lee, B. Full-color-tunable nanophotonic device using electrochromic tungsten trioxide thin film. *Nano Lett.* **2020**, *20*, 6084–6090. [[CrossRef](#)] [[PubMed](#)]
8. Geng, J.; Fang, X.; Zhang, L.; Yao, G.; Xu, L.; Liu, F.; Qiu, M. Controllable generation of large-scale highly regular gratings on Si films. *Light Adv. Manuf.* **2021**, *2*, 274–282. [[CrossRef](#)]
9. Soudi, M.; Cencillo-Abad, P.; Chanda, D. Plasmonic structural color-based sensors. In *Advanced Fabrication Technologies for Micro/Nano Optics and Photonics XVII*; SPIE: San Francisco, CA, USA, 2024.
10. Geng, J.; Shi, L.; Ni, J.; Jia, Q.; Yan, W.; Qiu, M. Wear-resistant surface coloring by ultrathin optical coatings. *Photonix* **2022**, *3*, 14. [[CrossRef](#)]
11. Zhang, C.; Chen, L.; Lin, Z.; Song, J.; Wang, D.; Li, M.; Koksall, O.; Wang, Z.; Spektor, G.; Carlson, D.; et al. Tantalum pentoxide: A new material platform for high-performance dielectric metasurface optics in the ultraviolet and visible region. *Light Sci. Appl.* **2024**, *13*, 23. [[CrossRef](#)] [[PubMed](#)]
12. Yang, W.; Xiao, S.; Song, Q.; Liu, Y.; Wu, Y.; Wang, S.; Tsai, D.P. All-dielectric metasurface for high-performance structural color. *Nat. Commun.* **2020**, *11*, 1864. [[CrossRef](#)] [[PubMed](#)]
13. Wu, Y.; Chen, Y.; Song, Q.; Xiao, S. Dynamic Structural Colors Based on All-Dielectric Mie Resonators. *Adv. Opt. Mater.* **2021**, *9*, 2002126. [[CrossRef](#)]
14. Wang, Y.; Yang, S.; Wang, X.; Xiang, H.; Lu, C.; Liu, X. Stretchable, stable, and structural color reversible enabled by mesoscopic regulation and design for flexible photonic crystal mechanical sensors. *Colloids Surf. A Physicochem. Eng. Asp.* **2024**, *689*, 133672. [[CrossRef](#)]
15. Liu, Y.; Liu, S.; Zhu, L.; Wu, Y.; Si, P.; Zhang, D. Harmless photonic crystal tattoo with angle-independent structural color based on SiO_2 nanoparticles and silk fibroin. *J. Appl. Polym. Sci.* **2024**, *141*, e55482. [[CrossRef](#)]
16. Liu, X.; Huang, Z.; Zang, J. All-dielectric silicon nanoring metasurface for full-color printing. *Nano Lett.* **2020**, *20*, 8739–8744. [[CrossRef](#)] [[PubMed](#)]
17. Li, K.; Li, T.; Zhang, T.; Li, H.; Li, A.; Li, Z.; Lai, X.; Hou, X.; Wang, Y.; Shi, L.; et al. Facile full-color printing with a single transparent ink. *Sci. Adv.* **2021**, *7*, eabh1992. [[CrossRef](#)]
18. Yang, Z.; Zhou, Y.; Chen, Y.; Wang, Y.; Dai, P.; Zhang, Z.; Duan, H. Reflective color filters and monolithic color printing based on asymmetric Fabry–Perot cavities using nickel as a broadband absorber. *Adv. Opt. Mater.* **2016**, *4*, 1196–1202. [[CrossRef](#)]
19. Xie, Y.; Song, Y.; Sun, G.; Hu, P.; Bednarkiewicz, A.; Sun, L. Lanthanide-doped heterostructured nanocomposites toward advanced optical anti-counterfeiting and information storage. *Light Sci. Appl.* **2022**, *11*, 150. [[CrossRef](#)]
20. Song, H.; Zhang, R.; Zhao, Z.; Wu, X.; Zhang, Y.; Wang, J.; Li, B. RGB tricolor and multimodal dynamic optical information encryption and decoding for anti-counterfeiting applications. *ACS Appl. Mater. Interfaces* **2022**, *14*, 45562–45572. [[CrossRef](#)]
21. Eoh, H.; Jung, Y.; Park, C.; Lee, C.E.; Park, T.H.; Kang, H.S.; Jeon, S.; Ryu, D.Y.; Huh, J.; Park, C. Photonic crystal palette of binary block copolymer blends for full visible structural color encryption. *Adv. Funct. Mater.* **2022**, *32*, 2103697. [[CrossRef](#)]
22. Wang, L.; Wang, T.; Yan, R.; Yue, X.; Wang, H.; Wang, Y.; Zhang, J.; Yuan, X.; Zeng, J.; Wang, J. Color printing and encryption with polarization-switchable structural colors on all-dielectric metasurfaces. *Nano Lett.* **2023**, *23*, 5581–5587. [[CrossRef](#)] [[PubMed](#)]
23. Xu, Y.; Wang, Y.; Yang, Y.; Yang, S.; Li, L.; Xiang, R.; Liu, J. Stretchable structural colors with polarization dependence using lithium niobate metasurfaces. *Opt. Express* **2024**, *32*, 6776–6790. [[CrossRef](#)] [[PubMed](#)]
24. Liu, Z.; Chen, Z.; Yang, S.; Jia, H.; Wei, J. Dual-Mode Multicolor Display Based on Structural and Fluorescent Color CdS Photonic Crystal Hydrogel. *Langmuir* **2024**, *40*, 4764072. [[CrossRef](#)]
25. Iwata, M.; Teshima, M.; Seki, T.; Yoshioka, S.; Takeoka, Y. Bio-inspired bright structurally colored colloidal amorphous array enhanced by controlling thickness and black background. *Adv. Mater.* **2017**, *29*, 1605050. [[CrossRef](#)] [[PubMed](#)]
26. Shang, L.; Zhang, W.; Xu, K.; Zhao, Y. Bio-inspired intelligent structural color materials. *Mater. Horiz.* **2019**, *6*, 945–958. [[CrossRef](#)]
27. Anusuyadevi, P.R.; Shanker, R.; Cui, Y.; Riazanova, A.V.; Järn, M.; Jonsson, M.P.; Svagan, A.J. Photoresponsive and polarization-sensitive structural colors from cellulose/liquid crystal nanophotonic structures. *Adv. Mater.* **2021**, *33*, 2101519. [[CrossRef](#)] [[PubMed](#)]

28. Fan, W.; Zeng, J.; Gan, Q.; Ji, D.; Song, H.; Liu, W.; Shi, L.; Wu, L. Iridescence-controlled and flexibly tunable retroreflective structural color film for smart displays. *Sci. Adv.* **2019**, *5*, eaaw8755. [[CrossRef](#)]
29. Yao, Y.; He, J.; Ma, L.; Wang, J.; Peng, L.; Zhu, X.; Li, K.; Qu, M. Self-supported Co₉S₈-Ni₃S₂-CNTs/NF electrode with superwetting multistage micro-nano structure for efficient bifunctional overall water splitting. *J. Colloid Interface Sci.* **2022**, *616*, 287–297. [[CrossRef](#)] [[PubMed](#)]
30. Neubrech, F.; Duan, X.; Liu, N. Dynamic plasmonic color generation enabled by functional materials. *Sci. Adv.* **2020**, *6*, eabc2709. [[CrossRef](#)] [[PubMed](#)]
31. ElKabbash, M.; Hoffman, N.; Lininger, A.R.; Jalil, S.A.; Letsou, T.; Hinczewski, M.; Strangi, G.; Guo, C. Fano resonant optical coatings platform for full gamut and high purity structural colors. *Nat. Commun.* **2023**, *14*, 3960. [[CrossRef](#)] [[PubMed](#)]
32. Chen, F.; Li, Y.; Yang, W.; Wang, B.; Xiao, S. WS₂ Monolayer in Fabry–Perot Cavity Support for Plasmonic Fano Resonance. *Plasmonics* **2023**, *18*, 1371–1380. [[CrossRef](#)]
33. Huang, Y.S.; Lee, C.Y.; Rath, M.; Ferrari, V.; Yu, H.; Woehl, T.J.; Ni, J.H.; Takeuchi, I.; Ríos, C. Tunable structural transmissive color in fano-resonant optical coatings employing phase-change materials. *Mater. Today Adv.* **2023**, *18*, 100364. [[CrossRef](#)]
34. Prabhathan, P.; Sreekanth, K.V.; Teng, J.; Singh, R. Electrically tunable steganographic nano-optical coatings. *Nano Lett.* **2023**, *23*, 5236–5241. [[CrossRef](#)]
35. Guan, X.; Liu, Q.; Li, C.; Yin, Z.; Wu, J.; Yu, P.; Lu, W.; Wang, S. Generalized Fano resonance theory based on Fabry-Perot cavity. *J. Phys. D Appl. Phys.* **2024**, *57*, 135102. [[CrossRef](#)]
36. Sreekanth, K.V.; Jana, S.; ElKabbash, M.; Singh, R.; Teng, J. Phase change material-based tunable Fano resonant optical coatings and their applications. *Nanophotonics* **2024**, *13*, 2075–2088. [[CrossRef](#)] [[PubMed](#)]
37. Morin, F.J. Oxides which show a metal-to-insulator transition at the Neel temperature. *Phys. Rev. Lett.* **1959**, *3*, 34–36. [[CrossRef](#)]
38. Fano, U. Effects of configuration interaction on intensities and phase shifts. *Phys. Rev.* **1961**, *124*, 1866. [[CrossRef](#)]
39. Currie, M.; Mastro, M.A.; Wheeler, V.D. Characterizing the tunable refractive index of vanadium dioxide. *Opt. Mater. Express* **2017**, *7*, 1697–1707. [[CrossRef](#)]
40. Palik, E.D. *Handbook of Optical Constants of Solids*; Elsevier Science: Amsterdam, The Netherlands, 1998; Volume 3, pp. 155–185.
41. Rakić, A.D.; Djurišić, A.B.; Elazar, J.M.; Majewski, M.L. Optical properties of metallic films for vertical-cavity optoelectronic devices. *Appl. Opt.* **1998**, *37*, 5271–5283. [[CrossRef](#)] [[PubMed](#)]

Disclaimer/Publisher’s Note: The statements, opinions and data contained in all publications are solely those of the individual author(s) and contributor(s) and not of MDPI and/or the editor(s). MDPI and/or the editor(s) disclaim responsibility for any injury to people or property resulting from any ideas, methods, instructions or products referred to in the content.